

# One-Pot Flash Combustion Synthesis, Structural, Morphological and Opto-Magnetic Properties of Spinel $Mn_xCo_{1-x}Al_2O_4$ ( $x = 0, 0.3, \text{ and } 0.5$ ) Nanocatalysts

A. Manikandan · M. Durka · S. Arul Antony

Received: 8 September 2014 / Accepted: 26 September 2014 / Published online: 7 October 2014  
© Springer Science+Business Media New York 2014

**Abstract** Spinel  $Mn_xCo_{1-x}Al_2O_4$  ( $x = 0, 0.3, \text{ and } 0.5$ ) nanoparticles were synthesized by a simple microwave-assisted combustion method. Powder X-ray diffraction (XRD) analysis was confirmed the formation of single phase, cubic spinel structure without other impurities. Average crystallite sizes of the samples were found to be in the range of 10.12 nm to 16.23 nm by Scherrer's method. FT-IR spectra showed the stretching frequencies corresponding to the M–Al–O bond of spinel structure. High-resolution scanning electron microscope (HR-SEM) and high-resolution transmission electron microscope (HR-TEM) images showed particle-like nanostructures. Band gap energy was estimated using UV-Visible DRS spectra and the values are increased with increasing  $Mn^{2+}$  content (3.45 eV to 3.75 eV). Vibrating sample magnetometer (VSM) measurements revealed that pure and Mn-doped  $CoAl_2O_4$  samples have ferromagnetic behavior and the magnetization values increased with increasing the concentration of  $Mn^{2+}$  ions in the  $CoAl_2O_4$  lattice. Catalytic oxidation of benzyl alcohol into benzaldehyde was found that the sample  $Mn_{0.5}Co_{0.5}Al_2O_4$  showed 96.58 % conversion with 100 % selectivity, whereas pure  $CoAl_2O_4$ , the conversion was only 87.43 % with 100 % selectivity.

**Keywords** Nanoparticles ·  $CoAl_2O_4$  · Electron microscopy · Optical properties · Magnetic properties · Catalytic properties

## 1 Introduction

Nanocrystalline spinels are a class of binary transition metal oxides that signify an attraction in the past decade; due to their small size, they exhibit novel physicochemical properties that lead to various potential applications [1–3]. Among various metal oxides, spinel cobalt aluminate ( $CoAl_2O_4$ ) has gained lot of interest in multidisciplinary areas, due to their effectiveness in ceramics, electronic, optical, catalyst, catalyst supports, aerospace, paints, dielectrics and sensing applications [4–7].  $CoAl_2O_4$  offers many favorable properties such as mechanical strength, thermal stability, low temperature sintering ability, high chemical stability, wide band-gap energy, excellent optical transparency, and good metal dispersion capacity [8, 9]. Spinel  $CoAl_2O_4$  is broadly used in paints for coloration, ceramics, enamels, paper, plastics, rubber and fibers [10].

Various methods have been used for the preparation of spinel  $CoAl_2O_4$  nanostructures such as low temperature, sol-gel, hydrolysis, and polymerized complex methods [11–13]. However, the above methods needed costly equipments and also claim costly materials that generate toxic organic/inorganic intermediates and laborious synthetic procedures, thus leading to the tedious polluting process. However, the main disadvantages of the above synthetic routes are required high temperature for calcinations to form the final products. Recently, a novel and facile method has been used to prepare nanostructured materials with high surface area, called microwave-assisted combustion method. In this method, the samples are prepared at low temperatures, low

A. Manikandan (✉) · S. Arul Antony (✉)  
PG and Research Department of Chemistry,  
Presidency College, Chennai 600 005, India  
e-mail: mkavath15@gmail.com  
e-mail: antonypresidency15@gmail.com

M. Durka  
Department of Physics, A.V.V.M Sri Pushpam College,  
Poondi, Tamil Nadu 613 503, India

cost with good control of size, structure, and morphology, due to its fast reaction kinetics, cleanliness and efficiency [14]. However, microwave-assisted combustion method is fast, simple, uniform heating, and energy efficient and has been widely used by many researchers [15, 16]. However, the microwave-assisted combustion method of preparation is easy, fast and has low energy with soft method than the above said methods [17]. As a result, morphology, surface area, crystallite size and other physicochemical properties can be altered. Furthermore, to our knowledge, no literature is available on the synthesis, optical, magnetic and catalytic properties of Mn-doped  $\text{CoAl}_2\text{O}_4$  nanostructures by a simple microwave-assisted combustion route.

Spinel  $\text{CoAl}_2\text{O}_4$  nanostructures have been used extensively as a heterogeneous catalyst and it can be recovered easily from the reaction mixture by simple filtration and reused several times. Moreover,  $\text{CoAl}_2\text{O}_4$  is nontoxic, inexpensive and has relatively high surface areas and these properties make them suitable for use as economically and environmentally viable solid heterogeneous catalysts. Generally, two main factors affecting the catalytic property of catalysts are the specific surface area and particle size, and typically, a high surface area goes along with small particle size, which enhances the catalytic activity [18, 19]. The as-prepared samples were characterized by X-ray diffraction (XRD), Fourier transform infrared (FT-IR) analysis, high-resolution scanning electron microscopy (HR-SEM), high-resolution transmission electron microscopy (HR-TEM), energy dispersive X-ray (EDX) spectroscopy, UV-Visible diffuse reflectance spectra (DRS), photoluminescence (PL) spectra, and vibrating sample magnetometer (VSM) techniques, and the obtained results are discussed. The product formed by the catalytic oxidation of benzyl alcohol to benzaldehyde was characterized by gas chromatography (GC). Catalytic activity tests of benzyl alcohol were carried out and reported the influence of  $\text{Mn}^{2+}$  dopant on catalytic activity of spinel  $\text{CoAl}_2\text{O}_4$  nanocatalysts. The best activity and selectivity towards catalytic oxidation of benzyl alcohol were observed.

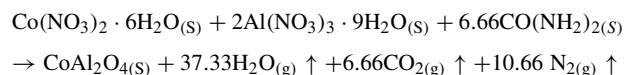
## 2 Experimental Part

### 2.1 Materials and Methods

All the chemicals used in this study were of analytical grade obtained from Merck, India, and were used as received without further purification. All chemicals such as nitrates of cobalt, manganese, aluminum, and urea as the fuel were used for this method. The samples were prepared with the addition of  $\text{Mn}^{2+}$  in different molar ratios ( $\text{Mn}_x\text{Co}_{1-x}\text{Al}_2\text{O}_4$ :  $x = 0.0, 0.3, \text{ and } 0.5$ ) to  $\text{CoAl}_2\text{O}_4$ . In case of  $\text{CoAl}_2\text{O}_4$ , the precursor mixture in urea was placed

in a domestic microwave oven and exposed to a microwave energy in a 2.45-GHz multimode cavity at 850 W for 10 min. When the solution attained the point of spontaneous combustion, ignition took place, resulting in a rapid flame and yielding solid fluffy final products of mixed metal oxides. The obtained solid powders were washed well with ethanol and dried at  $80^\circ\text{C}$  for 1 h, labeled as  $\text{CoAl}_2\text{O}_4$ ,  $\text{Mn}_{0.3}\text{Co}_{0.7}\text{Al}_2\text{O}_4$  and  $\text{Mn}_{0.5}\text{Co}_{0.5}\text{Al}_2\text{O}_4$ , respectively, and then used for further characterizations.

The expected microwave-assisted combustion reaction may be as follows:



### 2.2 Characterization Techniques

The structural characterization of spinel  $\text{Mn}_x\text{Co}_{1-x}\text{Al}_2\text{O}_4$  ( $x = 0.0, 0.3, \text{ and } 0.5$ ) samples was performed using a Rigaku Ultima X-ray diffractometer (XRD) for  $2\theta$  values ranging from  $10^\circ$  to  $80^\circ$  using  $\text{Cu-K}\alpha$  radiation ( $\lambda = 1.5418 \text{ \AA}$ ). The surface functional groups were analyzed by Perkin Elmer FT-IR spectrometer. The surface morphology of the samples was achieved at desired magnification with a Joel JSM 6360 highresolution scanning electron microscope (HR-SEM) equipped with energy dispersive X-ray (EDX) for elemental composition analysis. The transmission electron micrographs were carried out by Philips-TEM (CM20). The UV-visible diffuse reflectance spectrum (DRS) was recorded using Cary100 UV-visible spectrophotometer to estimate their band gap. The photoluminescence (PL) properties were recorded using Varian Cary Eclipse Fluorescence Spectrophotometer. Magnetic measurements were carried out at room temperature using a PMC Micro-Mag 3900 model vibrating sample magnetometer (VSM) equipped with 1 T magnet.

### 2.3 Catalytic Test

The oxidation of benzyl alcohol using spinel  $\text{Mn}_x\text{Co}_{1-x}\text{Al}_2\text{O}_4$  ( $x = 0.0, 0.3, \text{ and } 0.5$ ) samples was carried out in a batch reactor operated under atmospheric conditions. A 5 mmol of oxidant ( $\text{H}_2\text{O}_2$ ) was added along with 0.5 g of spinel  $\text{Mn}_x\text{Co}_{1-x}\text{Al}_2\text{O}_4$  catalysts ( $x = 0.0, 0.3, \text{ and } 0.5$ ), and the contents were heated at  $80^\circ\text{C}$  in an acetonitrile medium for 5 h in a three-necked round bottom flask equipped with a reflux condenser and thermometer. The oxidized products after the catalytic reaction are collected and studied using Agilent GC spectrometer. The column used for the study was DB wax column (capillary column) of

length 30 mm, and helium was used as the carrier gas. GC technique was carried out to know the conversion percentage of the products. The yields of the benzaldehyde formed were calculated by the following formulas (1) and (2) [19]:

$$\text{Conversion (\%)} = \frac{\text{Std. peak area} - \text{Sample peak area}}{\text{Sample peak area}} \times 100 \quad (1)$$

$$\text{Selectivity (\%)} = \frac{\text{Sample peak area}}{\text{Total peak area}} \times 100 \quad (2)$$

### 3 Results and Discussion

#### 3.1 Structural Analysis

The structure and phase purity of the samples were confirmed by analyzing the powder X-ray diffraction (XRD) patterns. Figure 1a–c shows the XRD patterns of spinel  $\text{Mn}_x\text{Co}_{1-x}\text{Al}_2\text{O}_4$  ( $x = 0.0, 0.3, \text{ and } 0.5$ ) nanoparticles, respectively. The characteristic peaks at  $2\theta$  of  $31.18^\circ, 36.82^\circ, 38.67^\circ, 44.59^\circ, 49.13^\circ, 55.77^\circ, 59.46^\circ, 65.57^\circ, 74.26^\circ$  and  $77.57^\circ$  are corresponds to (220), (311), (222), (400), (331), (422), (511), (440), (620) and (533) diffraction planes, respectively. According to the XRD patterns, all diffraction peaks can be perfectly indexed as centered cubic spinel structured  $\text{CoAl}_2\text{O}_4$  (JCPDS card no. 38-0814) [20]. The intensities and position of the peaks of the synthesized powders are in agreement with those of standard JCPDS and no other peak of any phase was detected, which indicates that the as-prepared samples were pure crystalline materials.

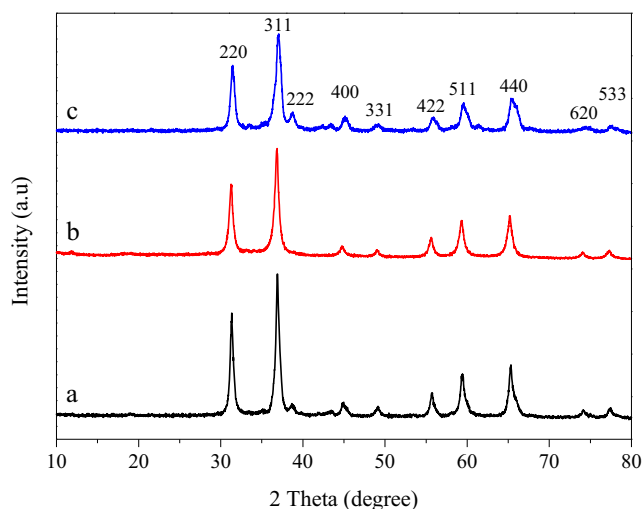


**Fig. 1** XRD patterns of **a**  $\text{CoAl}_2\text{O}_4$ , **b**  $\text{Mn}_{0.3}\text{Co}_{0.7}\text{Al}_2\text{O}_4$ , and **c**  $\text{Mn}_{0.5}\text{Co}_{0.5}\text{Al}_2\text{O}_4$  nanoparticles

The average crystallite size calculated from the most intense X-ray diffraction peak (311) using Scherrer's (3),

$$D = \frac{0.89\lambda}{\beta \cos \theta} \quad (3)$$

where  $D$  is the average crystallite size,  $\lambda$  the X-ray wavelength,  $\theta$  the Bragg diffraction angle, and  $\beta$  the full width at half maximum (FWHM). The average crystallite size was estimated by applying Scherrer's equation on the peak at  $2\theta = 36.82^\circ$  for all samples. The dependence of the average  $\text{CoAl}_2\text{O}_4$  crystallite sizes on the  $\text{Mn}^{2+}$  doping concentration is shown in the Table 1. It was found that the average crystallite size was higher (16.23 nm) for pure  $\text{CoAl}_2\text{O}_4$  while the crystallite size decreased from 13.74 to 10.12 nm for the Mn-doped  $\text{CoAl}_2\text{O}_4$  ( $x = 0.3$  to  $0.5$ , i.e.,  $\text{Mn}_{0.5}\text{Co}_{0.5}\text{Al}_2\text{O}_4$ ). It can be seen that the widths of peaks for the samples obtained at higher concentration of Mn dopant ( $\text{Mn}_{0.5}\text{Co}_{0.5}\text{Al}_2\text{O}_4$ ) are broader, indicating that the crystallite size is very small. The result reveal at Mn doping on  $\text{CoAl}_2\text{O}_4$  controls and retards the growth of the crystallite size.

#### 3.2 Fourier Transform Infrared Analysis

Figure 2a–c shows the FT-IR spectra of spinel  $\text{Mn}_x\text{Co}_{1-x}\text{Al}_2\text{O}_4$  ( $x = 0.0, 0.3, \text{ and } 0.5$ ) samples. A strong and broad absorption band centered in the region  $3000\text{--}3500\text{ cm}^{-1}$ , which can be assigned to the vibrations of water molecules. The absorption band at  $2345\text{ cm}^{-1}$  is due to the stretching vibration of  $\text{CO}_2$  from atmosphere. A band at around  $1631\text{ cm}^{-1}$  is present in all compositions, which can be assigned to the H–O–H bending vibration. The bands at  $660$  and  $552\text{ cm}^{-1}$  confirm the spinel structure of  $\text{CoAl}_2\text{O}_4$ . In all compositions of  $\text{CoAl}_2\text{O}_4$  samples, the metal-oxygen stretching frequencies are reported in the range  $500\text{--}700\text{ cm}^{-1}$ , associated with the vibrations of M–O, Al–O, and M–O–Al bonds ( $M = \text{Mn, Co}$ ) [21, 22]. The results are in good agreement with the results obtained from the XRD analysis.

**Table 1** Crystallite size, BET surface area and band gap values of spinel  $\text{Mn}_x\text{Co}_{1-x}\text{Al}_2\text{O}_4$  ( $x = 0.0, 0.3$  and  $0.5$ ) nanoparticles

Samples	Crystallite size (nm)	Band gap (eV)	BET surface area ( $\text{m}^2/\text{g}$ )
$\text{CoAl}_2\text{O}_4$	16.23	3.45	77.26
$\text{Mn}_{0.3}\text{Co}_{0.7}\text{Al}_2\text{O}_4$	13.74	3.66	80.42
$\text{Mn}_{0.5}\text{Co}_{0.5}\text{Al}_2\text{O}_4$	10.12	3.75	83.74

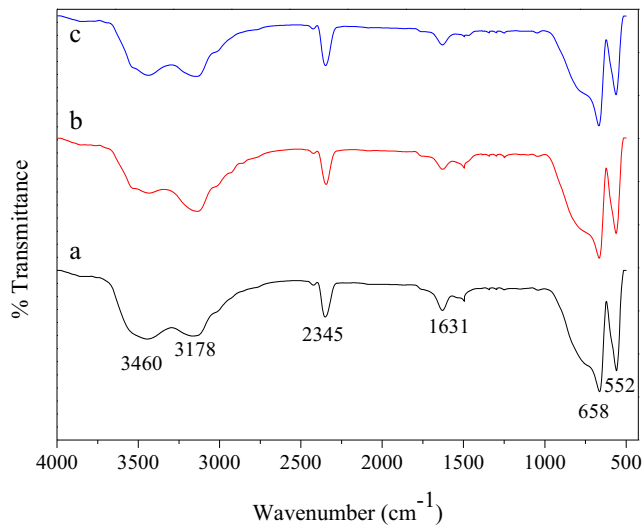
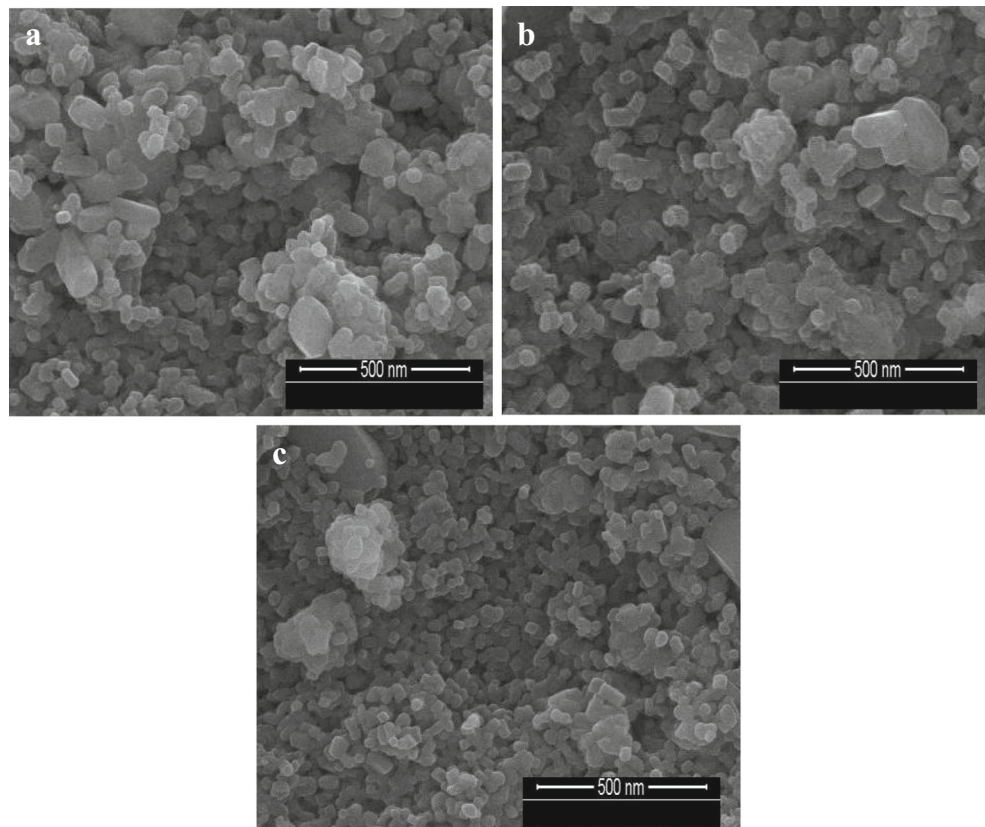


**Fig. 2** FT-IR spectra of **a**  $\text{CoAl}_2\text{O}_4$ , **b**  $\text{Mn}_{0.3}\text{Co}_{0.7}\text{Al}_2\text{O}_4$ , and **c**  $\text{Mn}_{0.5}\text{Co}_{0.5}\text{Al}_2\text{O}_4$  nanoparticles

### 3.3 Scanning Electron Microscopy Studies

The surface morphologies of the spinel  $\text{Mn}_x\text{Co}_{1-x}\text{Al}_2\text{O}_4$  ( $x = 0.0, 0.3, \text{ and } 0.5$ ) samples were confirmed by the high-resolution scanning electron microscopy (HR-SEM) analysis. Figure 3a–c shows HR-SEM images of  $\text{CoAl}_2\text{O}_4$ ,

**Fig. 3** HR-SEM images of **a**  $\text{CoAl}_2\text{O}_4$ , **b**  $\text{Mn}_{0.3}\text{Co}_{0.7}\text{Al}_2\text{O}_4$ , and **c**  $\text{Mn}_{0.5}\text{Co}_{0.5}\text{Al}_2\text{O}_4$  nanoparticles

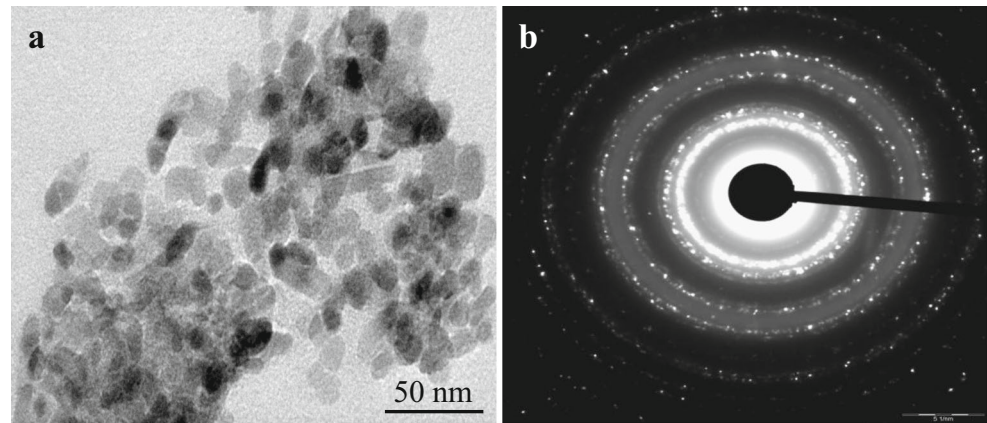


$\text{Mn}_{0.3}\text{Co}_{0.7}\text{Al}_2\text{O}_4$ , and  $\text{Mn}_{0.5}\text{Co}_{0.5}\text{Al}_2\text{O}_4$ , respectively. However, the surface morphologies of  $\text{Mn}_x\text{Co}_{1-x}\text{Al}_2\text{O}_4$  samples as seen from the HR-SEM images consist of particle-like nanostructures with uniform grain size smaller than 50 nm. It is believed that, during the combustion reaction, the microwave energy is used to nucleation growth of metallic  $\text{Co}^{2+}$  and  $\text{Al}^{3+}$  cation mixtures obtained with a very short time was subjected in the microwave irradiation treatment to formed products within few minutes of time with narrow size range was obtained [14]. The results proved that the microwave irradiation method is a fast and easy synthesis method, due to the microwave energy can directly interact with the material interior, which results in a well-developed nano-sized particles within a few minutes of time and there is no need for further calcinations.

### 3.4 Transmission Electron Microscopy Studies

The crystal structure, morphology, and particle size of the samples were confirmed by high-resolution transmission electron microscope (HR-TEM) analysis. Figure 4a show the HR-TEM images of  $\text{Mn}_{0.5}\text{Co}_{0.5}\text{Al}_2\text{O}_4$  sample. It was confirmed that the samples consists of particle-like nanostructures with small amount of agglomerations. However, these nanoparticles are in the range of 10–12 nm in diameter; these values are in good agreement with the values obtained

**Fig. 4** HR-TEM images **a** and SAED patterns **b** of  $\text{Mn}_{0.5}\text{Co}_{0.5}\text{Al}_2\text{O}_4$  nanoparticles



from XRD data. The selected area electron diffraction (SAED) pattern of the sample  $\text{Mn}_{0.5}\text{Co}_{0.5}\text{Al}_2\text{O}_4$ , presented in Fig. 4b, corresponds to that of the spinel phase confirmation. The SAED pattern implies that the as-prepared spinel  $\text{CoAl}_2\text{O}_4$  nanocrystals are good crystalline materials and single crystalline in nature.

### 3.5 Energy Dispersive X-ray Studies

Elemental composition of the samples was confirmed by energy dispersive X-ray (EDX) analysis. Figure 5a, b shows the EDX spectra of  $\text{CoAl}_2\text{O}_4$  and  $\text{Mn}_{0.5}\text{Co}_{0.5}\text{Al}_2\text{O}_4$ , respectively EDX results showed the peaks of Mn, Co, Al, and O elements in spinel  $\text{CoAl}_2\text{O}_4$  and  $\text{Mn}_{0.5}\text{Co}_{0.5}\text{Al}_2\text{O}_4$  samples respectively, and there is no other peak, which confirmed the as-prepared samples are pure. A small peak is appeared at 2.1 keV for both samples, which indicated the presence of gold (Au) peak, and it is has been used as a sputter (gold) coating, while preparing the sample for HR-SEM recording for the better visibility of the surface morphology.

### 3.6 $\text{N}_2$ Adsorption/Desorption Isotherms

Surface area and the adsorbance competence of  $\text{Mn}_x\text{Co}_{1-x}\text{Al}_2\text{O}_4$  nanocatalysts, BET analysis was carried out. BET surface area studies revealed the specific relation between the concentration of the adsorbate and its adsorption degree onto the adsorbent surface of the samples. It is well known that the surface area parameters of the samples varied according to the concentration of the Mn dopant on the  $\text{Mn}_x\text{Co}_{1-x}\text{Al}_2\text{O}_4$  nanocatalysts (Table 1). However, the sample  $\text{Mn}_{0.5}\text{Co}_{0.5}\text{Al}_2\text{O}_4$  has a higher surface area ( $83.74 \text{ m}^2/\text{g}$ ) than the other samples. In the microwave-assisted combustion synthesis process, an efficient and a homogeneous heating would result in a rapid and uniformity nucleation followed by the growth of spinel  $\text{Mn}_x\text{Co}_{1-x}\text{Al}_2\text{O}_4$  nanoparticles.

### 3.7 Diffuse Reflectance Spectroscopy

The fundamental process of UV-Visible absorption/reflectance/transmittance of light by nano-sized semi-

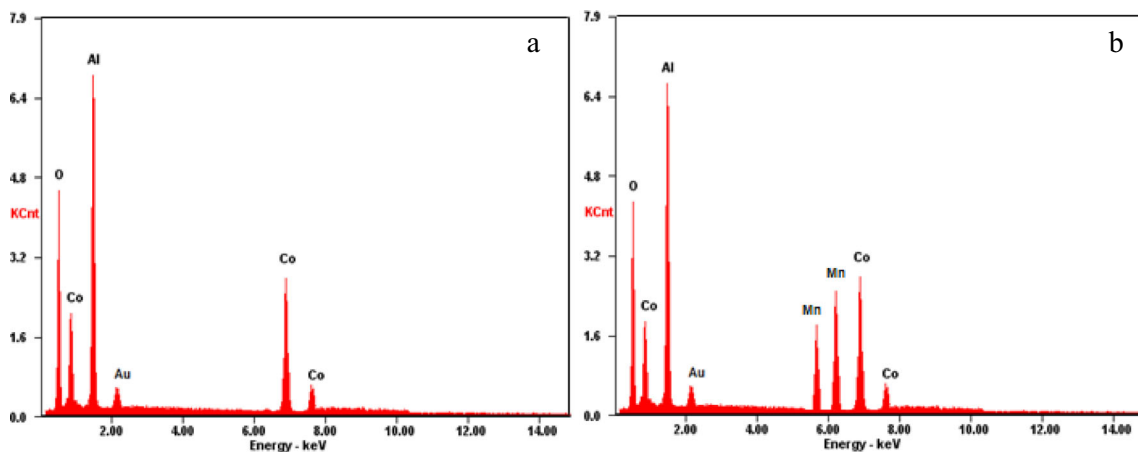


**Fig. 5** EDX spectra of **a**  $\text{CoAl}_2\text{O}_4$  and **b**  $\text{Mn}_{0.5}\text{Co}_{0.5}\text{Al}_2\text{O}_4$  nanoparticles

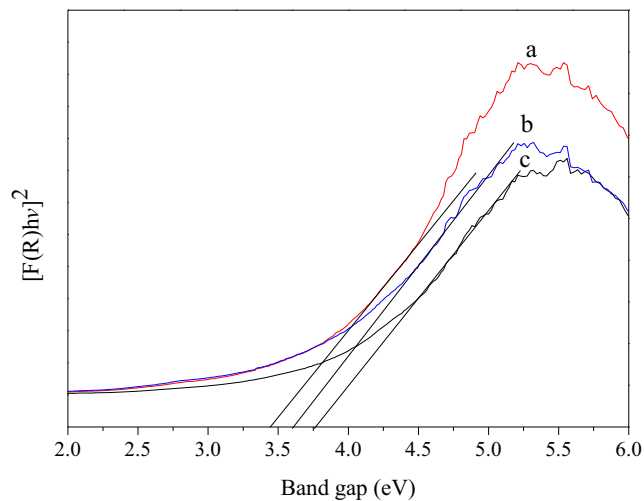


**Fig. 6** UV-Vis DRS spectra of **a**  $\text{CoAl}_2\text{O}_4$ , **b**  $\text{Mn}_{0.3}\text{Co}_{0.7}\text{Al}_2\text{O}_4$ , and **c**  $\text{Mn}_{0.5}\text{Co}_{0.5}\text{Al}_2\text{O}_4$  nanoparticles

conducting metal oxides is significant to their electronic structures. Hence, the UV-Visible diffuse reflectance spectroscopy (DRS) studies play a vital role in estimating the band gap energy of the semiconducting materials. The optical energy band gap was calculated using Tauc relation [23]. The Kubelka-Munk function is generally applied to convert the diffuse reflectance into equivalent absorption coefficient and mostly used for analyzing the powder samples [24]. The Kubelka-Munk function  $F(R)$  was used to calculate the band gap energy of the nanocrystalline  $\text{Mn}_x\text{Co}_{1-x}\text{Al}_2\text{O}_4$  samples. Thus, the vertical axis is converted into quantity  $F(R)$  which is equal to the absorption coefficient. Thus the

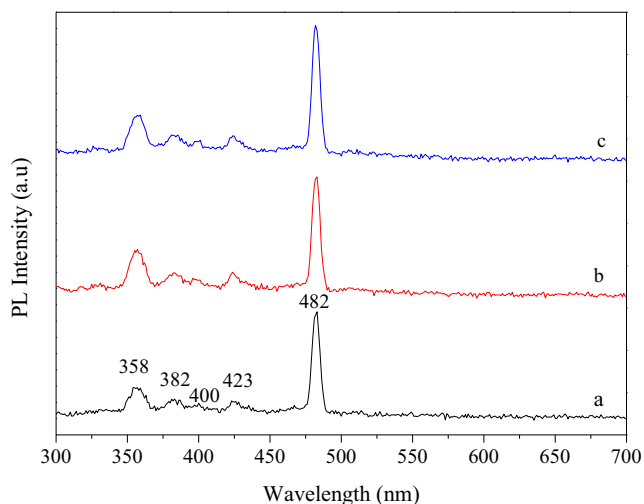


**Fig. 7** PL spectra of **a**  $\text{CoAl}_2\text{O}_4$ , **b**  $\text{Mn}_{0.3}\text{Co}_{0.7}\text{Al}_2\text{O}_4$ , and **c**  $\text{Mn}_{0.5}\text{Co}_{0.5}\text{Al}_2\text{O}_4$  nanoparticles

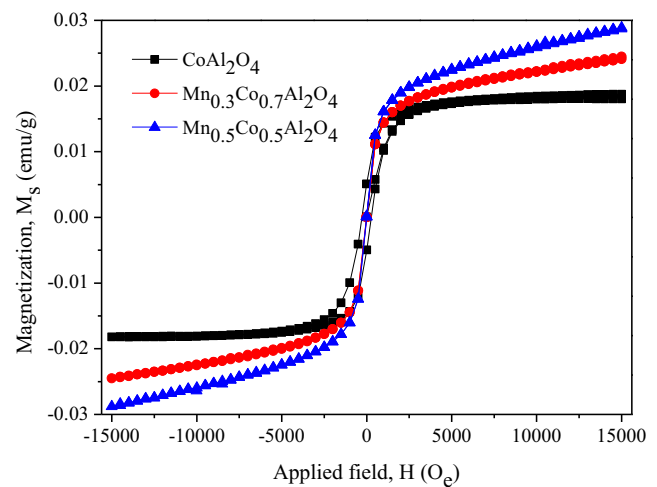


**Fig. 8** Magnetic hysteresis ( $M$ - $H$ ) loops of  $\text{Mn}_x\text{Co}_{1-x}\text{Al}_2\text{O}_4$  ( $x = 0.0, 0.3, \text{ and } 0.5$ ) nanoparticles

$\alpha$  in the Tauc equation is substituted with  $F(R)$  and hence the relation becomes,

$$(F(R)) = \alpha = \frac{(1 - R)^2}{2R} \quad (4)$$

where,  $F(R)$  is Kubelka-Munk function,  $\alpha$  the absorption coefficient, and  $R$  the reflectance. Thus the Tauc relation becomes,

$$F(R)h\nu = A(h\nu E_g)^n \quad (5)$$

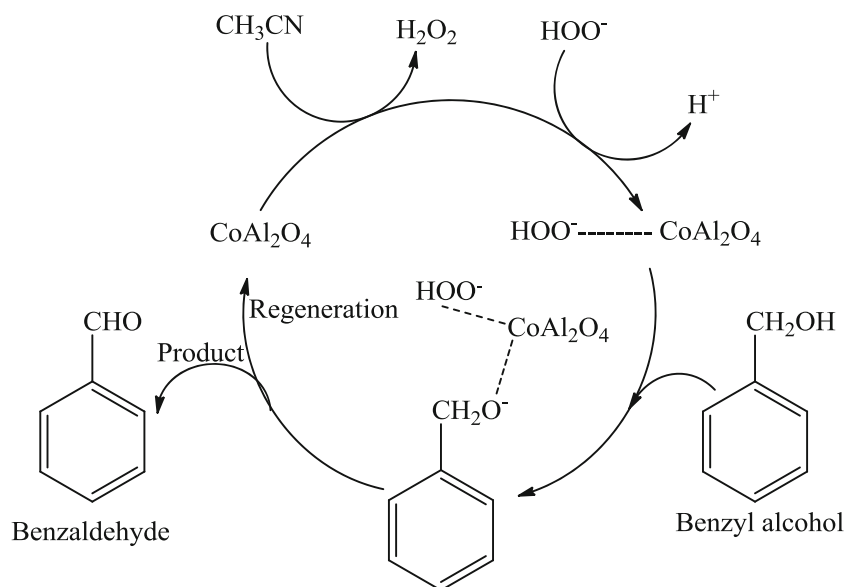
where  $n = 1/2$  and  $2$  for direct and indirect transitions, respectively, thus giving direct and indirect band gaps. The plots of  $(F(R)h\nu)^2$  versus  $h\nu$  for all compositions are shown in Fig. 6. Extrapolation of linear regions of these plots to  $(F(R)h\nu)^2 = 0$  gives the direct band gap values.

The optical band gap energy values for all composition of  $\text{Mn}_x\text{Co}_{1-x}\text{Al}_2\text{O}_4$  as shown in Table 1. The direct band gap value of the pure  $\text{CoAl}_2\text{O}_4$  was observed to be 3.45 eV, and it is increased with increasing the concentration of Mn dopant. The observed higher band gap energy of the pure

**Table 2** Magnetic properties (magnetization, remanence, and coercivity) of  $\text{Mn}_x\text{Co}_{1-x}\text{Al}_2\text{O}_4$  ( $x = 0.0, 0.3, \text{ and } 0.5$ ) nanoparticles

Samples	$H_c$ (Oe)	$M_r$ ( $\times 10^{-3}$ ) (emu/g)	$M_s$ ( $\times 10^3$ ) (emu/g)
$\text{CoAl}_2\text{O}_4$	94.68	1.457	18.46
$\text{Mn}_{0.3}\text{Co}_{0.7}\text{Al}_2\text{O}_4$	162.9	1.843	24.52
$\text{Mn}_{0.5}\text{Co}_{0.5}\text{Al}_2\text{O}_4$	212.5	5.314	29.13

**Scheme 1** Schematic diagram of catalytic oxidation of benzyl alcohol to benzaldehyde by spinel  $\text{Mn}_x\text{Co}_{1-x}\text{Al}_2\text{O}_4$  ( $x = 0.0, 0.3, \text{ and } 0.5$ ) nanoparticles



sample  $\text{CoAl}_2\text{O}_4$  is due to larger particle size [25]. Conversely, the band gap energy increased from 3.66 to 3.75 eV with increase in  $\text{Mn}^{2+}$  content ( $x = 0.3$  to 0.5) in  $\text{CoAl}_2\text{O}_4$  matrices, due to the increase of particle sizes. The increase of band gap energy may also be due to the *spd* exchange interaction between the localized *d* electrons of  $\text{Mn}^{2+}$  ions and band electrons of  $\text{CoAl}_2\text{O}_4$ . Thus, the contraction of band gap with Mn doping could be due to the formation of subbands in between the energy band gap and merging of their subbands with the conduction band to form a continuous band [26].

### 3.8 Photoluminescence Studies

Photoluminescence (PL) spectra were recorded to investigate the recombination phenomena of the semiconducting materials. Moreover, PL spectrum gives the information about the band gap with the relative active position of sub-band gap and defect states of the semiconductors [27, 28]. Generally,  $\text{CoAl}_2\text{O}_4$  is employed as the spinel type material and doped with transition metals (e.g. Cu and Mn) as the activator and co-activator. However, in this present study, we have reported the room temperature PL properties of spinel  $\text{CoAl}_2\text{O}_4$  doped with  $\text{Mn}^{2+}$ . Figure 7 demonstrates the room temperature PL spectra recorded at  $\lambda_{\text{ex}} = 290$  nm of  $\text{CoAl}_2\text{O}_4$  samples prepared with various doping concentrations of  $\text{Mn}^{2+}$  content. A small band is observed at 358 nm is ascribed to the near band-edge emission of wide band gap of  $\text{CoAl}_2\text{O}_4$  due to the recombination of free excitons through an exciton-exciton process.

The estimated band gap (3.45 eV) from the near band-edge emission is in agreement with the band gap estimated

from Kubelka-Munk plot derived from the DRS spectra. In the present study, spinel  $\text{Mn}_x\text{Co}_{1-x}\text{Al}_2\text{O}_4$  ( $x = 0.0, 0.3, \text{ and } 0.5$ ) samples show a peak corresponding to violet emission centered at 423 nm, due to the radiating defects related to the interface traps existing at the grain boundaries. Also, a blue emission (482 nm) appeared which represents a deep level visible emissions associated with localized levels in the band gap [29]. However, it is observed that the doping of  $\text{Mn}^{2+}$  in  $\text{CoAl}_2\text{O}_4$  spinel increases the luminescence intensity with an increase the Mn dopant. Thus, the results are suggested that the various emissions in the  $\text{Mn}_x\text{Co}_{1-x}\text{Al}_2\text{O}_4$  spinel arise, due to the defect centers that act as trap levels, which lead to the appearance of new electronic energy levels between the valence and the conduction band [30].

### 3.9 VSM Measurements

The magnetic behavior of spinel  $\text{Mn}_x\text{Co}_{1-x}\text{Al}_2\text{O}_4$  ( $x = 0.0, 0.3, \text{ and } 0.5$ ) nanoparticles was investigated by using the external magnetic field between  $\pm 15$  kOe using room temperature vibrating sample magnetometer (VSM). Magnetizations ( $M$ ) versus magnetic field ( $H$ ) behavior plots are shown in Fig. 8. The observed saturation magnetization ( $M_s$ ), remanent magnetization ( $M_r$ ), and coercivity ( $H_c$ ) values are reported in Table 2. These  $MH$  curves are typical for a soft magnetic material and indicate ferromagnetism in the field ranges of  $\pm 15$  kOe. All the Mn-doped  $\text{CoAl}_2\text{O}_4$  ( $x = 0.0, 0.3 \text{ and } 0.5$ ) nanoparticles display 'hysteresis' type curve and the magnetization increases with increasing  $\text{Mn}^{2+}$  ions. The obtained result shows that the value of  $M_s$  is lower ( $18.46 \times 10^3$  emu/g) for pure  $\text{CoAl}_2\text{O}_4$ , and it is

increased from  $24.52 \times 10^3$  emu/g to  $29.13 \times 10^3$  emu/g with increase the concentration of  $\text{Mn}^{2+}$  ( $x = 0.3$  to  $0.5$ ), which can be attributed to the high magnetic nature of  $\text{Mn}^{2+}$  ions ( $5 \mu_B$ ) substituted by the lower magnetic moments of  $\text{Co}^{2+}$  ( $3 \mu_B$ ) ions in the spinel  $\text{CoAl}_2\text{O}_4$  lattice [31–33]. However, it is observed that the lower  $H_c$  and  $M_r$  values confirm that the  $\text{CoAl}_2\text{O}_4$  nanoparticles have soft and weak ferromagnetic nature, due to the exchange between the ions occupying the tetrahedral and octahedral sites [34, 35].

### 3.10 Catalytic Tests

It is well known that the catalytic activity of nanomaterials depends strongly on particle size, morphology and structure. Nanomaterials have been receiving increased attention, because they exhibit unusual properties that are significantly different from those of relatively larger particles of the same materials [36]. These unusual properties have been attributed to the extremely small sizes and the high specific surface areas of the nanoparticles. In the present study, the liquid phase catalytic oxidation of benzyl alcohol into benzaldehyde was carried out using the spinel  $\text{Mn}_x\text{Co}_{1-x}\text{Al}_2\text{O}_4$  ( $x = 0.0, 0.3$ , and  $0.5$ ) nanocatalysts. Catalytic studies showed that the nature and concentration of the dopant ions had a strong influence on both the conversion and product selectivity (Scheme 1). The catalytic results were summarized in Table 3.

Generally, the catalyst with a high specific surface area has a favorable effect on the catalytic activity. In this present work, the surface area of the  $\text{Mn}_x\text{Co}_{1-x}\text{Al}_2\text{O}_4$  ( $x = 0.0, 0.3$ , and  $0.5$ ) nanocatalysts gradually increased with the increase of  $\text{Mn}^{2+}$  content ( $x = 0.5$ ). However, the sample  $\text{Mn}_{0.5}\text{Co}_{0.5}\text{Al}_2\text{O}_4$  had a higher surface area ( $83.74 \text{ m}^2/\text{g}$ ) than the other samples, due to the smaller size of  $\text{Mn}_{0.5}\text{Co}_{0.5}\text{Al}_2\text{O}_4$  samples. Furthermore, the sample  $\text{Mn}_{0.5}\text{Co}_{0.5}\text{Al}_2\text{O}_4$  nanocatalyst showed better catalytic activity than the other samples (Fig. 9). However, the high specific surface area of  $\text{Mn}_{0.5}\text{Co}_{0.5}\text{Al}_2\text{O}_4$  nanoparticle was useful to catalytic activity via enhancing the adsorption of

**Table 3** The conversion and selectivity percentage for the oxidation of benzyl alcohol to benzaldehyde (reaction conditions: catalyst ( $\text{Mn}_x\text{Co}_{1-x}\text{Al}_2\text{O}_4$ :  $x = 0.0, 0.3$ , and  $0.5$ ),  $0.5 \text{ g}$ ; benzyl alcohol,  $5 \text{ mmol}$ ; acetonitrile,  $5 \text{ mmol}$ ;  $\text{H}_2\text{O}_2$ ,  $5 \text{ mmol}$ ; temperature,  $80 \text{ }^\circ\text{C}$ ; time,  $5 \text{ h}$ )

Samples	Conversion (%)	Selectivity (%)
$\text{CoAl}_2\text{O}_4$	87.43	100
$\text{Mn}_{0.3}\text{Co}_{0.7}\text{Al}_2\text{O}_4$	90.73	100
$\text{Mn}_{0.5}\text{Co}_{0.5}\text{Al}_2\text{O}_4$	96.58	100

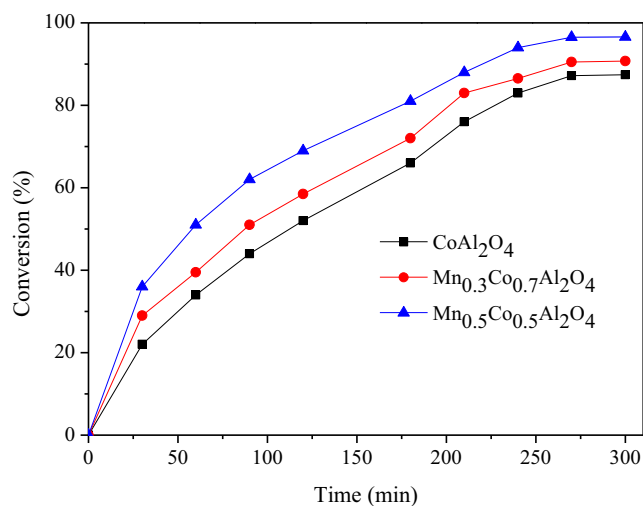


**Fig. 9** Catalytic activities (reaction conditions: catalyst ( $\text{Mn}_x\text{Co}_{1-x}\text{Al}_2\text{O}_4$ :  $x = 0.0, 0.3$ , and  $0.5$ ),  $0.5 \text{ g}$ ; benzyl alcohol,  $5 \text{ mmol}$ ; acetonitrile,  $5 \text{ mmol}$ ;  $\text{H}_2\text{O}_2$ ,  $5 \text{ mmol}$ ; temperature,  $80 \text{ }^\circ\text{C}$ ; time,  $5 \text{ h}$ )

benzyl alcohol, which is the determining step in the catalytic reaction. It was found that the conversion of benzyl alcohol to benzaldehyde for the sample  $\text{Mn}_{0.5}\text{Co}_{0.5}\text{Al}_2\text{O}_4$  was  $96.58 \%$  with  $100 \%$  selectivity, whereas for the pure  $\text{CoAl}_2\text{O}_4$ , the conversion was only  $87.43 \%$  with  $100 \%$  selectivity. However, the  $\text{Mn}_{0.5}\text{Co}_{0.5}\text{Al}_2\text{O}_4$  nanocatalyst with high surface area displays the best performance in the selective oxidation of benzyl alcohol to benzaldehyde. Besides, as the particle size decreases, the number of surface active sites increases in the catalysts. Thus, it is expected

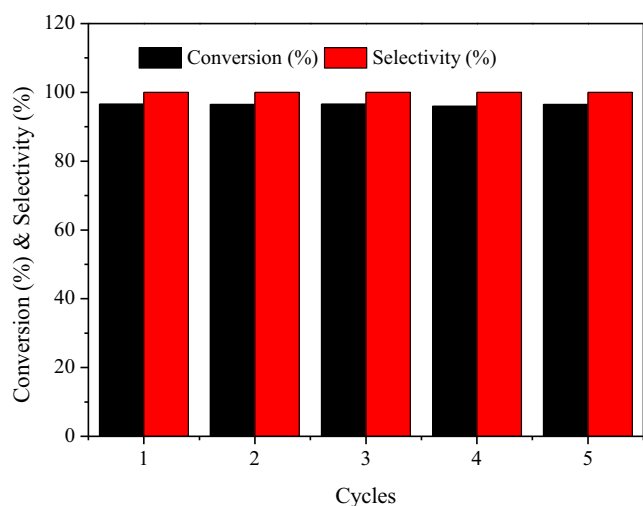


**Fig. 10** The reusability of the spinel  $\text{Mn}_{0.5}\text{Co}_{0.5}\text{Al}_2\text{O}_4$  catalyst for the catalytic oxidation of benzyl alcohol to benzaldehyde



that the sample  $\text{Mn}_{0.5}\text{Co}_{0.5}\text{Al}_2\text{O}_4$  nanoparticles with very smaller particle size distribution would be a potentially efficient catalyst, due to the larger surface area coverage and better adsorption behavior, which in turn leads to the efficient catalysis [37].

### 3.11 Reusability Studies

The catalytic oxidation of benzyl alcohol to benzaldehyde was employed as a model reaction to investigate the reusability of spinel  $\text{Mn}_{0.5}\text{Co}_{0.5}\text{Al}_2\text{O}_4$  nanocatalyst. The recycling of the catalyst is very important for industrial and technological applications. The reusability of the catalyst for the liquid phase oxidation of benzyl alcohol to benzaldehyde was evaluated, and the results are shown in Fig. 10. For the reusability study purpose, the sample  $\text{Mn}_{0.5}\text{Co}_{0.5}\text{Al}_2\text{O}_4$  nanoparticles was filtered off from each run and washed several times with ethanol and dried at 110 °C in an air oven for 2 h and was checked for five consecutive runs under the identical conditions. During the five runs investigated, the conversion of benzyl alcohol was in a range from 96.51 to 96.46 % for the sample  $\text{Mn}_{0.5}\text{Co}_{0.5}\text{Al}_2\text{O}_4$ , indicating that these catalysts display good reproducibility and stability. Interestingly, the formation of benzoic acid was not detected. Since the spinel  $\text{Mn}_{0.5}\text{Co}_{0.5}\text{Al}_2\text{O}_4$  nanocatalyst is able to oxidize benzyl alcohol to benzaldehyde with high activity, highly recyclable, remarkably stable, and environmental friendly, they are promising candidates for the industrial applications.

## 4 Conclusions

Spinel  $\text{Mn}_x\text{Co}_{1-x}\text{Al}_2\text{O}_4$  ( $x = 0.0, 0.3, \text{ and } 0.5$ ) nanocatalysts were successfully prepared by a simple microwave-assisted combustion method using urea as the fuel. Effects of  $\text{Mn}^{2+}$  doping on structural, morphological and optomagnetic properties were investigated and also the catalytic activity for the selective oxidation of benzyl alcohol was investigated. Powder XRD, EDX and SAED results indicate that the as-synthesized samples have the spinel structure without any other phase impurities. The appearance of two bands between 500 and 700  $\text{cm}^{-1}$  in FT-IR spectra revealed the formation of M–O, Al–O, and M–O–Al bonds in the spinel structure. HR-SEM and HR-TEM images depicted the formation of well developed particle-like morphology with nanosized grains below 50 nm. UV-Visible DRS results showed the band gap value of pure  $\text{CoAl}_2\text{O}_4$  is 3.45 eV, and it increase from 3.66 to 3.75 eV with increasing the Mn dopant ( $x = 0.3$  to 0.5). VSM studies revealed that the

pure and  $\text{Mn}^{2+}$  in  $\text{CoAl}_2\text{O}_4$  showed ferromagnetic behavior. It was found that the sample  $\text{Mn}_{0.5}\text{Co}_{0.5}\text{Al}_2\text{O}_4$  is highly active towards the selective oxidation of benzyl alcohol to benzaldehyde with the conversion of 96.58 % with 100 % selectivity.

**Acknowledgments** One of the authors, A. Manikandan is thankful to CSIR, New Delhi, India, for the award of Senior Research Fellowship (CSIR-SRF).

## References

- Zhai, M., Ye, S., Xia, Z., Liu, F., Qi, C., Shi, X., Wang, G.: J. Supercond. Nov. Magn. **27**, 1861 (2014)
- Kurmude, D.V., Kale, C.M., Aghav, P.S., Shengule, D.R., Jadhav, K.M.: J. Supercond. Nov. Magn. **27**, 1889 (2014)
- Koseoglu, Y.: Ceram. Int. **39**, 4221 (2013)
- Davis, M., Gumeci, C., Alsup, R., Korzeniewski, C., Weeks, L.J.H.: Mater. Lett. **73**, 139 (2012)
- Kumar, M., Seshagiri, T.K., Mohapatra, M., Natarajan, V., Godbole, S.V.: J. Lumin. **132**, 2810 (2012)
- Pandey, R., Gale, J.D., Sampath, S.K., Recio, J.M.: J. Am. Ceram. Soc. **82**, 3337 (1999)
- Song, J., Leng, M., Fu, X., Liu, J.: J. Alloys Compd. **543**, 142 (2012)
- Zawadzki, M.: Solid State Sci. **8**, 14 (2006)
- Davar, F., Niasari, M.S.: J. Alloys Compd. **509**, 2487 (2011)
- Kurajica, S., Popovic, J., Tkalec, E., Grzeta, B., Mandic, V.: Mater. Chem. Phys. **135**, 587 (2012)
- Zayat, M., Levy, D.: Chem. Mater. **12**, 2763 (2000)
- Yu, F.L., Ma, Y., Du, J.Y., Zhou, J.: J. Alloys Compd. **468**, 443 (2009)
- Li, W.D., Li, J.Z., Guo, J.K.: J. Eur. Ceram. Soc. **23**, 2289 (2003)
- Koseoglu, Y.: Ceram. Int. **40**, 4673 (2014)
- Suliman, I.E., Eftekhari, H., Mohseni, S.M., Tehranchi, M.M.: J. Supercond. Nov. Magn. **24**, 1263 (2011)
- Jin, M., Wang, Z., Jiang, H., Sun, Y., Wang, X., Qian, H., Chen, Q., Liu, K. J. Supercond. Nov. Magn. **26**, 2779 (2013)
- Visinescu, D., Jurca, B., Ianculescu, A., Carp, O.: Polyhedron **30**, 2824 (2011)
- Ge, D.L., Fan, Y.J., Qi, C.L., Sun, Z.X.: J. Mater. Chem. A **1**, 1651 (2013)
- Manikandan, A., Sridhar, R., Antony, S.A., Ramakrishna, S.: J. Mol. Struct. **1076**, 188 (2014)
- Walerczyk, W., Zawadzki, M., Grabowska, H.: Catal. Lett. **141**, 592 (2011)
- Sigel, G.A., Bartlett, R.A., Decker, D., Olmstead, M.M., Power, P.P.: Inorg. Chem. **26**, 1773 (1987)
- Ramirez, J.P., Mul, G., Kapteijn, F., Moulijn, J.A.: J. Mater. Chem. **11**, 821 (2001)
- Wang, S.F., Gu, F., Lu, M.K., Cheng, X.F., Zou, W.G., Zhou, G.J., Wang, S.M., Zhou, Y.Y.: J. Alloys Compd. **394**, 255 (2005)
- Bai, H., Liu, Z., Sun, D.D.: Int. J. Hydrogen Energy **37**, 13998 (2012)
- Jamal, E.M.A., Kumar, D.S., Anantharaman, M.R.: Bull. Mater. Sci. **34**, 251 (2011)

26. Ahmed, A.S., Muhamed, S.M., Singk, M.L., Tabassum, S., Naqvi, A.H., Azam, A.: *J. Lumin.* **131**, 1 (2011)
27. Schmidt, T., Lischka, K., Zulehner, W.: *Phys. Rev. B* **45**, 8989 (1992)
28. Sendi, R.K., Mahmudm, S.: *Appl. Surf. Sci.* **258**, 8026 (2012)
29. Bhargava, R., Sharma, P.K., Dutta, R.K., Kumar, S., Pandey, A.C., Kumar, N.: *Mater. Chem. Phys.* **120**, 393 (2010)
30. Shen, Y., Li, W., Li, T.: *Mater. Lett.* **65**, 2956 (2011)
31. Ferreira, N.S., Abracado, L.G., Macedo, M.A.: *J. Supercond. Nov. Magn.* **26**, 2549 (2013)
32. Xu, L., Zhang, H., Shen, K., Xu, M., Xu, Q.: *J. Supercond. Nov. Magn.* **25**, 1951 (2012)
33. Manikandan, A., Arul Antony, S.: *J. Supercond. Nov. Magn.* (2014). doi:[10.1007/s10948-014-2634-9](https://doi.org/10.1007/s10948-014-2634-9)
34. Ichiyangi, Y., Kimishima, Y., Yamada, S.: *J. Magn. Magn. Mater.* **272**, E1245 (2004)
35. Bhatt, A.S., Bhat, D.K., Tai, C., Santosh, M.S.: *Mater. Chem. Phys.* **125**, 347 (2011)
36. Karaoglu, E., Baykal, A.: *J. Supercond. Nov. Magn.* **27**, 2041 (2014)
37. Baykal, A., Karaoglu, E., Sozeri, H., Uysal, E., Toprak, M.S.: *J. Supercond. Nov. Magn.* **26**, 165 (2013)